



HAL
open science

The influence of transverse motion within an atomic gravimeter

Anne Louchet-Chauvet, Tristan Farah, Quentin Bodart, André Clairon,
Arnaud Landragin, Sébastien Merlet, Franck Pereira dos Santos

► **To cite this version:**

Anne Louchet-Chauvet, Tristan Farah, Quentin Bodart, André Clairon, Arnaud Landragin, et al..
The influence of transverse motion within an atomic gravimeter. *New Journal of Physics*, 2011, 13,
pp.5025. 10.1088/1367-2630/13/6/065025 . hal-03784966

HAL Id: hal-03784966

<https://hal.science/hal-03784966>

Submitted on 30 Sep 2022

HAL is a multi-disciplinary open access archive for the deposit and dissemination of scientific research documents, whether they are published or not. The documents may come from teaching and research institutions in France or abroad, or from public or private research centers.

L'archive ouverte pluridisciplinaire **HAL**, est destinée au dépôt et à la diffusion de documents scientifiques de niveau recherche, publiés ou non, émanant des établissements d'enseignement et de recherche français ou étrangers, des laboratoires publics ou privés.



Distributed under a Creative Commons Attribution 4.0 International License

OPEN ACCESS

The influence of transverse motion within an atomic gravimeter

To cite this article: Anne Louchet-Chauvet *et al* 2011 *New J. Phys.* **13** 065025

View the [article online](#) for updates and enhancements.

You may also like

- [SEI Characterization Using Ferrocene/Ferrocenium As Redox Shuttle](#)
Minh-Thu Dinh Nguyen and Charles Delacourt
- [Climate-change impact potentials as an alternative to global warming potentials](#)
Miko U F Kirschbaum
- [Quasi-probability distributions in loop quantum cosmology](#)
Jasiel Berra-Montiel and Alberto Molgado

The influence of transverse motion within an atomic gravimeter

Anne Louchet-Chauvet¹, Tristan Farah, Quentin Bodart, André Clairon, Arnaud Landragin, Sébastien Merlet and Franck Pereira Dos Santos²

LNE-SYRTE, Observatoire de Paris, CNRS and UPMC, 61 avenue de l'Observatoire de Paris, F-75014 Paris, France

E-mail: franck.pereira@obspm.fr

New Journal of Physics **13** (2011) 065025 (20pp)

Received 15 February 2011

Published 28 June 2011

Online at <http://www.njp.org/>

doi:10.1088/1367-2630/13/6/065025

Abstract. Limits on the long-term stability and accuracy of a second generation cold atom gravimeter are investigated. We demonstrate a measurement protocol based on four interleaved measurement configurations, which allows rejection of most of the systematic effects, but not those related to Coriolis acceleration and wave-front distortions. Both are related to the transverse motion of the atomic cloud. Carrying out measurements with opposite orientations with respect to the Earth's rotation vector direction allows us to separate the effects and correct for the Coriolis shift. Finally, measurements at different atomic temperatures are presented and analyzed. In particular, we show the difficulty of extrapolating these measurements to zero temperature, which is required in order to correct for the bias due to wave-front distortions.

¹ Present address: Laboratoire Aimé, Cotton, CNRS UPR3321, University Paris Sud, Bâtiment 505, Campus Universitaire, 91405 Orsay, France.

² Author to whom any correspondence should be addressed.

Contents

1. Introduction	2
2. The cold atom gravimeter	3
3. Measurement of the gravity: protocol and results	4
3.1. Principle	4
3.2. Protocol	5
3.3. Long-term measurements	6
4. Systematic effects related to transverse trajectories	8
4.1. Detection	9
4.2. Coriolis shift evaluation	11
4.3. Stability of the cloud position, and the effect on g	13
4.4. Estimation of the optical aberrations bias	14
5. Conclusion	17
Acknowledgments	19
References	19

1. Introduction

Atom interferometry realizes inertial sensors of high performances, which compete with the state of the art instruments. Among these, gravimeters [1] are of interest for a wide range of applications, from geophysics [2], prospection to fundamental physics [3, 4]. The level of maturity of this technology enables the industrial development of such sensors [5], based on simplified geometries [6], with improved compactness and robustness with respect to laboratory-based instruments, whose ultimate performances are still to be met. We present here a study on the accuracy and long-term stability of an atomic gravimeter, developed in the frame of the watt balance project of the Laboratoire National de Métrologie et d'Essais (LNE), which aims at measuring the Planck constant with a relative accuracy of the order of 10^{-8} [3]. The target accuracy of this gravimeter is $1 \mu\text{Gal}$.³ This setup is a second-generation experiment that allows us to overcome some of the limits identified with a first prototype [7]. It has been recently compared to classical corner cube gravimeters. Reasonable agreement between the instruments was found in a large key comparison organized at BIPM [8] as well as in comparisons at the LNE laboratory involving two to three instruments [9, 10]. As an example, in [9] the difference was found to be $(4.3 \pm 6.4) \mu\text{Gal}$. Yet, the differences between these different instruments and/or between different measurements realized by the cold atom gravimeter at the same station can amount to $15 \mu\text{Gal}$, which is marginally compatible with the instruments uncertainties. We attribute these differences and their fluctuations to the influence of systematic effects related to the transverse motion of the atoms in the interferometer, which are the subject of this paper.

We first describe in section 2 the main features of the experimental setup. Section 3 presents the principle of the measurement of g and the specific protocol we use in order to reject a large class of systematic shifts. A long continuous g measurement is then presented and the long-term stability of the gravimeter is evaluated. Section 4 focuses on two remaining systematic effects which are difficult to separate: the Coriolis acceleration and the wave-front distortion

³ $1 \mu\text{Gal} = 10^{-8} \text{ m s}^{-2}$.

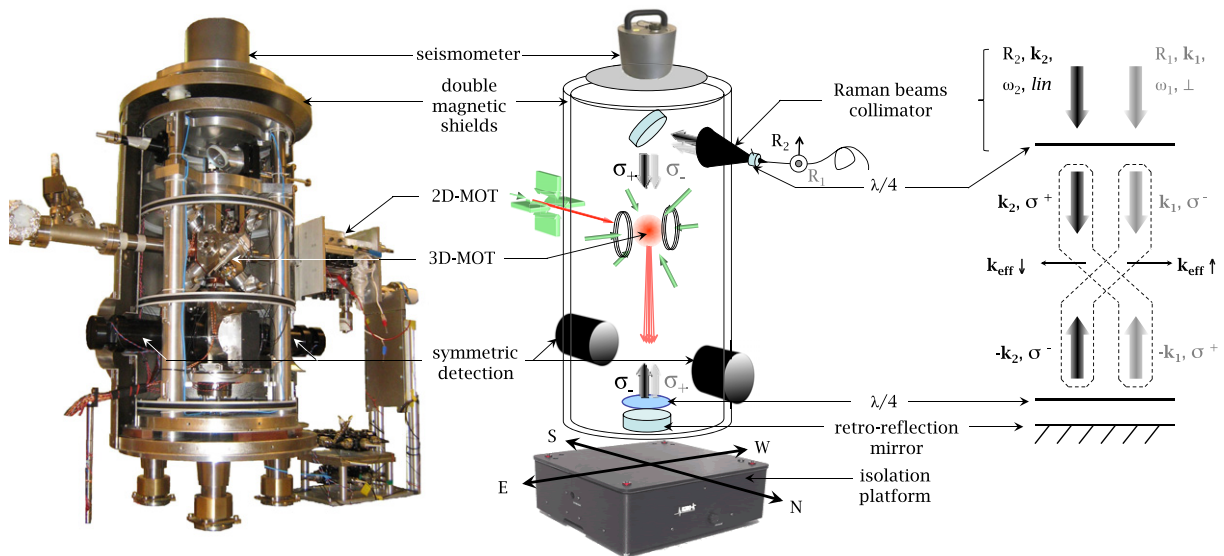


Figure 1. Left and center: photograph and schematic diagram of the cold atom gravimeter chamber with magnetic shields partially removed on the photograph (25 dB reduction). The 3D magneto-optical trap is in the upper area, composed of two horizontal beams in the East–West direction and four beams in the North–South plane. The free fall height is about 16 cm in a cylinder of diameter 40 mm from the 3D-MOT to the detection area at the bottom. In addition, a CCD camera (not represented) watches the 3D-MOT from the North–West. Right: configuration of the Raman laser beams. Two pairs of σ^-/σ^- and σ^+/σ^+ counter-propagating lasers allow us to induce Raman transitions with an effective wave vector k_{eff} pointing upwards or downwards. The Raman collimator aperture is 28 mm.

shifts. Both are related to the transverse trajectories of the atoms, which might not be weighted equally by the detection system. This motivated the development of a homogeneous detection system, which is described in detail in section 4.1. A careful study of the Coriolis acceleration phase shift is then realized in section 4.2 and the impact of trajectory fluctuations on the stability of the g measurement is evaluated in section 4.3. Finally, wave-front distortions are probed in section 4.4, using measurements realized for increasing atomic temperatures. We finally discuss the difficulty of extrapolating g measurements to zero temperature.

2. The cold atom gravimeter

The scheme of our cold atom gravimeter is presented in figure 1. It carries out a cyclic measurement of the gravity acceleration g with a cloud of ^{87}Rb cold atoms used as a test mass, with a repetition rate of about 3 Hz.

At first, about 10^8 atoms are loaded within 80 ms in a three-dimensional magneto-optical trap (3D-MOT) from the intense beam of a 2D-MOT. After a far-detuned optical molasses phase (up to 20Γ during 3 ms with an intensity of 0.8 mW cm^{-2}), the lasers are adiabatically switched off within $200 \mu\text{s}$ and the atoms fall at a temperature of $2 \mu\text{K}$. A narrow vertical velocity distribution of width (FWHM) of about 1 cm s^{-1} is then selected in the $|F = 1, m_F = 0\rangle$

state with a combination of microwave and optical Raman pulses. Two milliseconds later, the interferometer is realized with a sequence of three Raman pulses ($\pi/2 - \pi - \pi/2$), which split, redirect and recombine the atomic wave packets. These pulses are separated by free evolution times of $T = 70$ ms. The Raman pulses, which couple the hyperfine levels $|F = 1\rangle$ and $|F = 2\rangle$ of the $^5S_{1/2}$ ground state via two-photon excitation [11], are induced by two vertical counter-propagating laser beams of frequencies ω_1, ω_2 and wave vectors \vec{k}_1, \vec{k}_2 . Finally, thanks to the state labeling method [12], we deduce the interferometer phase shift from a fluorescence measurement of the populations of each of the two states. The transition probability P from one hyperfine state to the other is given by $P = \frac{1}{2}(1 + C \cos \Delta\Phi)$, where C is the interferometer contrast, and $\Delta\Phi$ the difference of the atomic phases accumulated along the two paths. When neglecting the gravity gradient [1], this phase difference is given by $\Delta\Phi_g = \varphi_1 - 2\varphi_2 + \varphi_3 = -\vec{k}_{\text{eff}} \cdot \vec{g}T^2$ [13], where φ_i is the Raman laser phase difference at the i th pulse and $\vec{k}_{\text{eff}} = \vec{k}_1 - \vec{k}_2$ is the effective wave vector (with $|\vec{k}_{\text{eff}}| = |\vec{k}_1| + |\vec{k}_2|$ for counter-propagating beams).

We use the detection scheme tested in the previous prototype [7], which was inspired by the detection system [14] of the gradiometer [15]. It consists in using the vertical laser beams to first freeze, and then illuminate at full power, the atoms in front of the fluorescence collection optics. We carry out simultaneous population measurements of the two hyperfine states on independent photodiodes from which we derive the normalized transition probability. This geometry suppresses common mode intensity and frequency fluctuations of the vertical laser beam. More details of the collection setup will be given in section 4.1.

The Raman laser geometry is presented in figure 1. The two laser beams are first overlapped and injected into a common fiber, and delivered to the atoms through a single collimator with a $1/e^2$ waist of 12 mm, a clear aperture of 28 mm and an intensity of 16 mW cm^{-2} . The counter-propagating beams are obtained with a mirror and a quarter-wave plate placed inside the UHV chamber (both specified to $\lambda/20$). This technical solution produces four beams onto the atoms. Due to conservation of angular momentum and to the Doppler shift induced by the free fall of the atoms, only two counter-propagating beams will drive the Raman transitions according to the two-photon resonance condition given by

$$\omega_1 - \omega_2 = \omega_{\text{HFS}} + \frac{\vec{p} \cdot \vec{k}_{\text{eff}}}{m_{\text{Rb}}} + \omega_{\text{R}} + \delta^{\text{AC}}, \quad (1)$$

where ω_{HFS} is the hyperfine splitting, $\omega_{\text{R}} = \hbar|\vec{k}_{\text{eff}}|^2/2m_{\text{Rb}}$ the recoil pulsation, m_{Rb} the mass of ^{87}Rb , \vec{p} the momentum and δ^{AC} the differential light shift between the two hyperfine levels [16]. The Doppler term $\omega_{\text{D}} = \vec{p} \cdot \vec{k}_{\text{eff}}/m_{\text{Rb}}$ allows us to choose between the two pairs of beams to realize the Raman transitions with a wave-vector pointing upwards (k_{\uparrow}) or downwards (k_{\downarrow}).

The gravimeter chamber lies on top of a passive isolation platform, in order to reduce the influence of parasitic vibrations. In addition, the interferometer phase $\Delta\Phi$ is post-corrected from the effect of the remaining vibration noise [7], which is measured independently with a low-noise seismometer (Guralp T40) rigidly attached to the vacuum chamber.

3. Measurement of the gravity: protocol and results

3.1. Principle

The Raman lasers come from two extended cavity diode lasers based on the design described in [17] and amplified by two independent tapered amplifiers. They are phase-locked onto a

low-phase-noise microwave reference source, which is swept according to $\omega_2 - \omega_1 = \omega_2(0) - \omega_1(0) + \alpha t$ in order to compensate for the Doppler shift induced by gravity. This adds a αT^2 term to the interferometer phase, which eventually cancels for a perfect Doppler compensation. The central fringe of the interferometer thus corresponds to $\alpha_0 = \vec{k}_{\text{eff}} \cdot \vec{g}$. The value of g is therefore derived from the frequency chirp and from the mean effective wave-vector. We use a positive (resp. negative) frequency chirp to build an interferometer with k_{\downarrow} (resp. k_{\uparrow}).

Maximal sensitivity to phase fluctuations is achieved when operating the interferometer at half-fringe, which corresponds to $\Delta\Phi = \pm\pi/2$. The Raman phase is modulated by $\pm\pi/2$ so that the measurement is always carried out at half-fringe height, alternately on both sides of the central fringe. From two consecutive measurements of the transition probability P_i and P_{i+1} , the phase error can be estimated. In practice, a correction $G \times (P_i - P_{i+1})$ is added at each cycle to α , in order to stir the chirp rate onto the central fringe. This realizes an integrator, whose time constant can be set to a few cycles by adjusting the gain G . This locking technique has the advantage of rejecting offset and contrast fluctuations, while preserving maximal sensitivity to phase fluctuations.

3.2. Protocol

The measurement of g is shifted by systematic effects. These systematic phase shifts can be sorted into two classes of error sources, either dependent ($\Delta\Phi_{\text{dep}}$) or not dependent ($\Delta\Phi_{\text{indep}}$) on the direction of \vec{k}_{eff} . The difference of the atomic phases accumulated along the two paths of the interferometer can thus be expressed as $\Delta\Phi_g = -\vec{k}_{\text{eff}} \cdot \vec{g}T^2 + \Delta\Phi_{\text{dep}} + \Delta\Phi_{\text{indep}}$. Taking that into account, the measurement procedure we use interleaved g measurements with k_{\uparrow} and k_{\downarrow} :

$$\begin{aligned}\Delta\Phi_{\uparrow} &= k_{\text{eff}}gT^2 + \Delta\Phi_{\text{dep}} + \Delta\Phi_{\text{indep}}, \\ \Delta\Phi_{\downarrow} &= -k_{\text{eff}}gT^2 - \Delta\Phi_{\text{dep}} + \Delta\Phi_{\text{indep}}.\end{aligned}\quad (2)$$

Half-difference and half-sum of successive $\Delta\Phi_{\uparrow}$ and $\Delta\Phi_{\downarrow}$ measurements allow us to separate $\Delta\Phi_{\text{indep}}$ from $k_{\text{eff}}gT^2 + \Delta\Phi_{\text{dep}}$. $\Delta\Phi_{\text{indep}}$ originates from effects related to perturbations of the internal degrees of freedom of the atoms (such as magnetic field gradient and one-photon light shift) and from the radiofrequency phase shifts [1]. $\Delta\Phi_{\text{dep}} = \Delta\Phi_{\text{C}} + \Delta\Phi_{\text{WF}} + \Delta\Phi_{\text{LS2}}$ with $\Delta\Phi_{\text{C}}$ being the Coriolis phase shift, $\Delta\Phi_{\text{WF}}$ the wave-front aberration phase shift and $\Delta\Phi_{\text{LS2}}$ the two-photon light shift. $\Delta\Phi_{\text{LS2}}$ is due to off-resonant Raman transitions, which shift the atomic levels and therefore modify the hyperfine transition frequency [18]. As it scales linearly with the Rabi frequency of the Raman lasers Ω_{eff} , additional measurements realized with half-Rabi frequency allow us to correct for this effect by extrapolating to zero. Finally, the algorithm contains four configurations measuring, respectively, $\Delta\Phi_{\uparrow, \Omega_{\text{eff}}}$, $\Delta\Phi_{\downarrow, \Omega_{\text{eff}}}$, $\Delta\Phi_{\uparrow, \Omega_{\text{eff}}/2}$ and $\Delta\Phi_{\downarrow, \Omega_{\text{eff}}/2}$. They allow us to determine the following four linear combinations:

$$\Delta\Phi_{\uparrow, \Omega_{\text{eff}}/2} - \Delta\Phi_{\downarrow, \Omega_{\text{eff}}/2} - \frac{\Delta\Phi_{\uparrow, \Omega_{\text{eff}}} - \Delta\Phi_{\downarrow, \Omega_{\text{eff}}}}{2} = \Delta\Phi_g + \Delta\Phi_{\text{C}} + \Delta\Phi_{\text{WF}}, \quad (3)$$

$$2[(\Delta\Phi_{\uparrow, \Omega_{\text{eff}}} - \Delta\Phi_{\downarrow, \Omega_{\text{eff}}}) - (\Delta\Phi_{\uparrow, \Omega_{\text{eff}}/2} - \Delta\Phi_{\downarrow, \Omega_{\text{eff}}/2})] = \Delta\Phi_{\text{LS2}}, \quad (4)$$

$$\text{and for } i = \Omega_{\text{eff}} \text{ and } \Omega_{\text{eff}}/2, \quad \frac{\Delta\Phi_{\uparrow, i} + \Delta\Phi_{\downarrow, i}}{2} = \Delta\Phi_{\text{indep}} \quad (5)$$

with $\Delta\Phi_g = k_{\text{eff}}gT^2$.

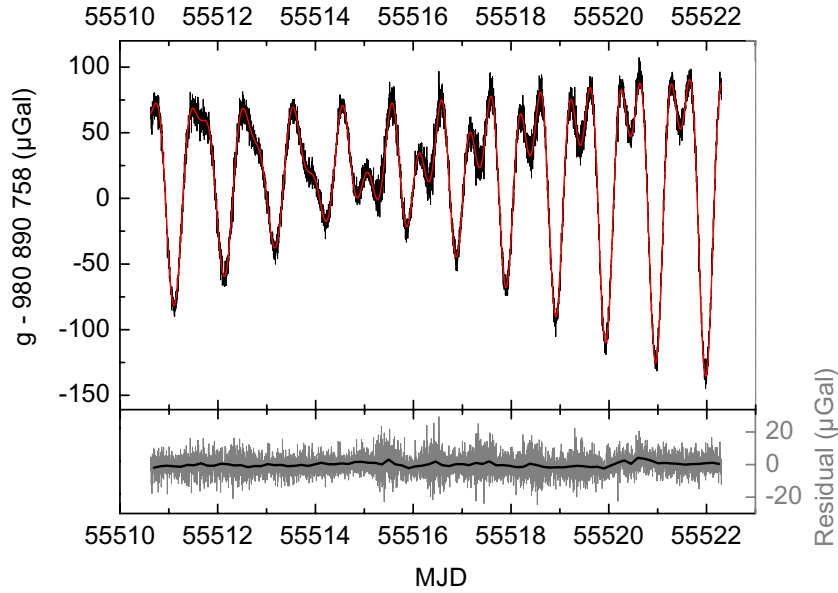


Figure 2. Top: continuous g measurement from 10 to 22 November 2010 uncorrected for tides (bins of 400 drops). Red solid line: tide model. Bottom: residuals, in gray for bins of 400 drops (170 s) and in black for bins of 10 000 s.

This algorithm thus allows us to carry out g measurements ideally only affected by Coriolis and the wave-front aberrations effects. While alternating k_{\uparrow} and k_{\downarrow} configurations does not degrade the sensitivity in the g measurement, the arithmetic involved when canceling the two-photon light shift leads to a degradation of the short-term sensitivity by a factor $\sqrt{10}$ with respect to a single configuration measurement. Indeed, as the sensitivity of a single configuration measurement $\sigma_{\Delta\Phi_g}$ is independent of the pointing direction of \vec{k}_{eff} and of the Rabi frequency Ω_{eff} , summing quadratically the uncorrelated sensitivities $\sigma_{\Delta\Phi}$ of the left-hand terms in equation (3) leads to a sensitivity on $\Delta\Phi_g$ of $\sqrt{5/2} \times \sigma_{\Delta\Phi}$. As each $\Delta\Phi_g$ is obtained with four measurement points, it corresponds to an effective cycle time of $4T_c$, where T_c is the cycle time of the experiment. This leads to a global degradation of the sensitivity of $\sqrt{5/2} \times \sqrt{4} = \sqrt{10}$ with respect to a single configuration measurement.

Both $\Delta\Phi_C$ and $\Delta\Phi_{\text{WF}}$ depend on the transverse trajectories of the atoms and are thus difficult to distinguish clearly. We will focus on them in sections 4.2 and 4.4, respectively.

3.3. Long-term measurements

Figure 2 shows a continuous g measurement carried out for 12 days in November 2010. It was carried out in our laboratory dedicated to gravity measurements [19] close to the LNE watt balance project [3] near Paris. The points represented on this figure are obtained switching from one configuration to the next every 100 shots. Each point thus represents 400 drops (about 170 s). Only three outliers out of 6000 points over the 12 day measurement have been withdrawn from the figure. The measurements have been corrected for atmospheric pressure and polar motion effect on g [20] but not for tides, which they follow in very good agreement with a local tidal model [19]. The residuals obtained by correcting the data for tides are represented at the bottom of the figure for bins of 170 and 10 000 s. We see resolved temporal

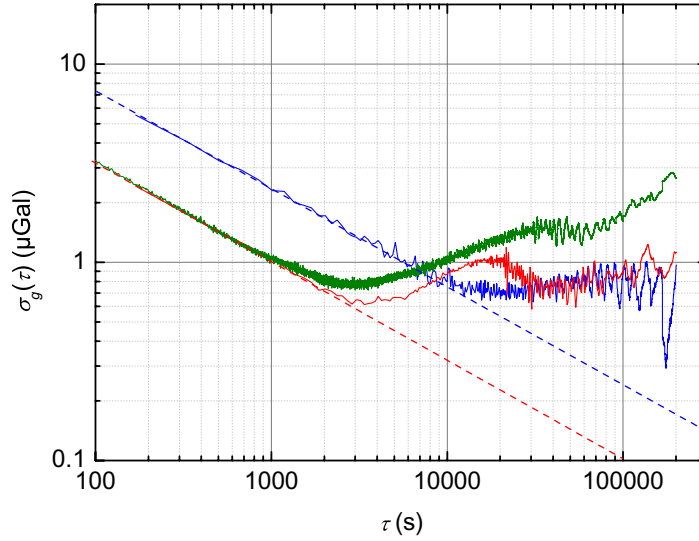


Figure 3. Allan standard deviation of the residual. Blue line: using the four-configuration algorithm to reject the LS2. Red and green lines: using only two configurations alternating k_{\uparrow} and k_{\downarrow} . Half-difference is represented in red and half-sum in green. They correspond to a red slope $\sqrt{5/2}$ lower than the blue one.

changes in the noise, which we attribute to variations in human activity over nights and days or weekends.

The Allan standard deviation of the residual signal is represented as a blue line in figure 3. It averages down as white noise in $\tau^{-1/2}$ and corresponds to an equivalent sensitivity at 1 s of $\sigma_g = 70 \mu\text{Gal}$. The sensitivity remains lower than $1 \mu\text{Gal}$ after 5000 s and flickers at the level of $0.7\text{--}0.8 \mu\text{Gal}$, which is comparable to the accuracy of our local tidal model [19]. It is thus difficult to assess whether the long-term stability is limited by our instrument or by the tidal model itself. On the same figure, the red line (resp. green line) represents the Allan standard deviation of the half-difference (resp. of the half-sum) when alternating only two configurations k_{\uparrow} and k_{\downarrow} . Note that for these two curves we selected data only at full intensity, which amounts to taking only half of the data points, keeping the same effective cycle time of $4T_c$. The green curve shows the instability of the phase shifts that are independent of the direction of \vec{k}_{eff} ($\Delta\Phi_{\text{indep}}$ according to equation (5)). The algorithm suppresses these fluctuations and allows us to obtain a sensitivity of $0.6 \mu\text{Gal}$ after 3000 s. Nevertheless the measurement is still sensitive to the two-photon light shift fluctuations represented by the bump on the red curve at about 18 000 s. Finally, the improvement in stability for long-term measurement with four interleaved configurations clearly illustrates the efficiency of the two-photon light shift rejection.

In figure 4, we present 43 other determinations performed at the same position in the room⁴ over the last year, shown as a white circle, the result of the 12 day measurement from figure 2. We observe a dispersion of $3 \mu\text{Gal}$ around the mean value of $980\,890\,755 \mu\text{Gal}$. The white squares represent the values obtained during the intercomparison presented in [10]. Our mean value lies $10 \mu\text{Gal}$ above the weighted mean value obtained by corner cube gravimeters at the same position since 2006 [9, 10, 21], which could be due to the optical wave-front, which is

⁴ The measurements have been carried out in position GR₄₀, which is a reference station at the Center of the Gravimetry Laboratory [19].

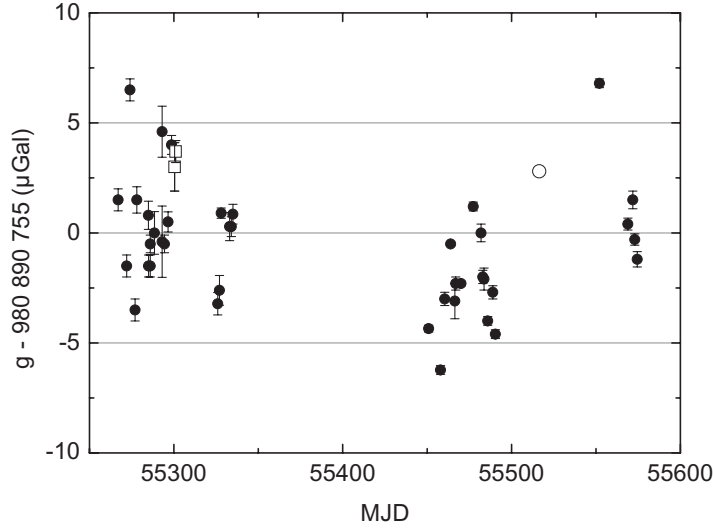


Figure 4. g absolute measurements from March 2010 to January 2011. The white circle corresponds to the measurement presented in figure 2. White squares present the measurements during the comparison in April 2010 [10]. The error bars represent the statistical uncertainties.

still to be evaluated. Indeed, the data in figure 4 are corrected for the different systematic effects already mentioned and for Coriolis acceleration using the procedure described in section 4.2, but not for the effect of wave-front aberrations. The study of the impact of the last two effects is the topic of the following sections.

4. Systematic effects related to transverse trajectories

Due to its finite temperature T_{at} , the atomic cloud expands during free fall. Atoms with a nonzero transverse velocity are sensitive both to Coriolis acceleration and to wave-front distortions (figure 5), which makes it difficult to determine independently the two associated phase shifts, $\Delta\Phi_{\text{C}}$ and $\Delta\Phi_{\text{WF}}$.

Firstly, for an atom with an initial velocity in the horizontal plane, the interferometer arms enclose a spatial area, which makes it sensitive to rotations via the Sagnac effect [22, 23]. In particular, for an initial atomic velocity \vec{v}_{\perp} along the East–West direction, this additional phase shift due to the Earth’s rotation leads to a bias in the g measurement of $\Delta g = -2\vec{\Omega}_{\text{T}} \wedge \vec{v}_{\perp}$. This Coriolis shift is an odd function of v_{\perp} . It can thus be averaged to zero if the velocity distribution is perfectly symmetric, centered around zero velocity, and if the fluorescence detection is symmetric too (figure 5(b)). For a cloud with $T_{\text{at}} = 2 \mu\text{K}$, a homogeneity of 1% is needed to determine g with a relative accuracy of 10^{-9} .

Secondly, the phase shift due to aberrations depends on the details of the wave-front distortions convoluted with the atomic trajectories. For an atom with a nonzero radial velocity, the phase at each pulse thus depends on the trajectory in a nontrivial way. In our experiment, the Raman laser phase difference is only sensitive to perturbations induced by the retro-reflecting optics (the mirror and the quarter-wave plate), which are noncommon to the upwards and downwards beams (figure 5(c)). As a case study, for a parabolic curvature of the wave-front

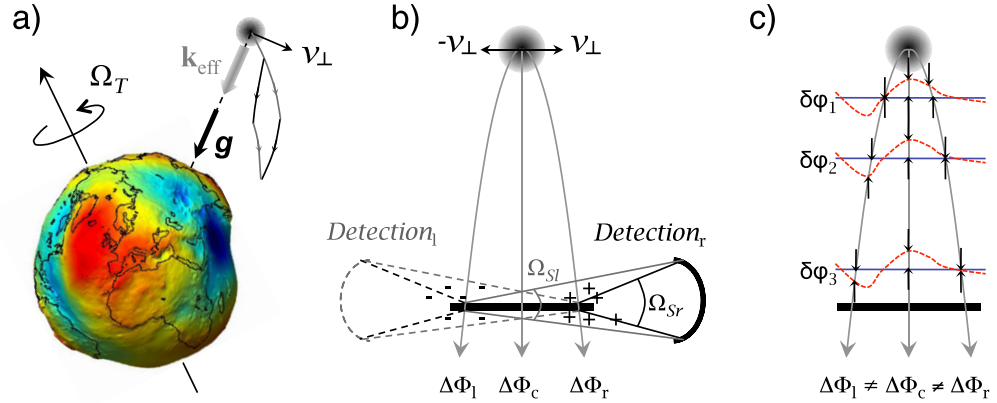


Figure 5. Systematic effects related to the cloud expansion. (a) Schematic representation of the Coriolis effect. For an atom with a nonzero transverse velocity $v_{\perp} \neq 0$, a spatial area opens during the interferometer leading to a Sagnac phase shift. (b) Dispersion of the atoms position in the fluorescence detection zone due to the ballistic expansion. With a single-side collection optical system, $Detection_r$ on the right, atoms with a velocity v_{\perp} have more impact on the measurement than those with a speed $-v_{\perp}$ due to the difference in solid angles Ω . Using a second system placed on the left restores the symmetry. (c) Propagation of the atomic cloud in an imperfect wave-front. For an atom whose trajectory is not perfectly vertical, the phases at the three pulses are different, leading to a systematic shift. The mean effect results from the convolution of this shift over the position and velocity distributions.

$\Delta\Phi = Kr^2$, we obtain

$$\Delta\Phi_{Ab} = 2K\sigma_v^2 T^2 = \frac{k_{\text{eff}} k_B T_{\text{at}}}{R m_{\text{Rb}}} T^2, \quad (6)$$

where σ_v is the rms velocity, assuming the distribution is a Maxwell Boltzmann distribution. R is the radius of the curvature and k_B Boltzmann constant. With $T_{\text{at}} = 2 \mu\text{K}$ the radius of curvature should be larger than 20 km for a bias $\Delta g < 10^{-9}g$ (this corresponds to a flatness better than the $\lambda/300$ peak valley over a beam diameter of 10 mm). Note that the phase evolution along the vertical direction due to the propagation of the Gaussian laser beams also induces a bias due to the Gouy phase and to the evolution of the radius of curvature R [24]. In the case of our Raman beam with large $1/e^2$ diameter (24 mm) and radius of curvature ($R = 6$ km), the effect is dominated by the Gouy phase contribution and is calculated to be lower than $0.1 \mu\text{Gal}$.

4.1. Detection

In the vertical detection scheme, detection homogeneity is ensured by the large diameter of the vertical Raman beam ($1/e^2$ waist of 12 mm), which is much larger than the atomic cloud in the detection area ($\sigma_r = 2$ mm) and by the large saturation parameter ($s = 60$). This corresponds to a homogeneity in the fluorescence scattering rate better than 1% over $\pm 3\sigma$. The fluorescence collection is performed with four photodetectors placed symmetrically on either side of the vacuum chamber, along the North–South axis. The optical arrangement is based on a

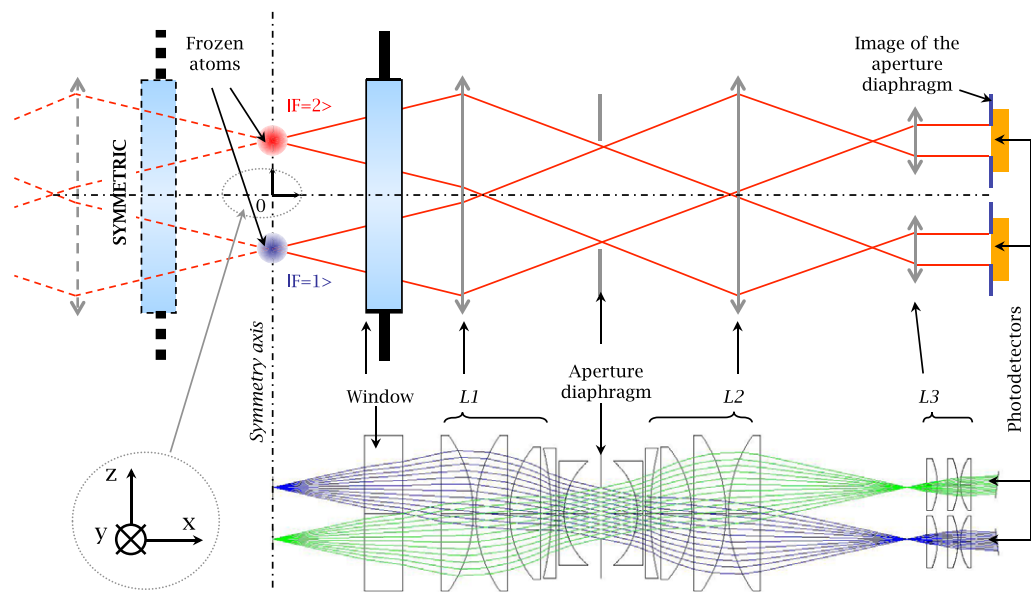


Figure 6. Optical setup for the collection of atomic fluorescence. The two atomic clouds are represented in red for $|F = 2\rangle$ and in blue for $|F = 1\rangle$. The x - and y -axes correspond to the North–South and East–West directions, respectively.

double-Gauss [25] system and shown in figure 6. A first optical group L_1 collimates the fluorescence beam, and a second group L_2 forms the image of the source. An aperture is placed in the focal plane of group L_1 , which sends the image of the input pupil at infinity. This kind of setup ensures that the atom cloud is always seen in the same direction, whatever its position. A third optical group L_3 images the aperture on the photodetector in such a way that the atoms close to the axis always illuminate the same area of the detector. The measurement is then insensitive to the inhomogeneity of the photodiode. The system was designed to achieve a collection efficiency of 1% and a homogeneity in the horizontal plane of about 1% over $1\text{ cm} \times 1\text{ cm}$.

Before their implementation onto the chamber, the two detection systems have been characterized. The photodiode responses were measured as a function of the position of a light source, which was moved around the atomic cloud position in the three directions x , y and z represented in figure 6. This light source was realized by illuminating a diffusing plate with a 1 mm diameter collimated beam.

Figure 7 (left) displays the signals measured by the two photodetectors in one such detection setup for a horizontal displacement along y , the light source being centered in the other two directions at the position that will correspond to the upper atomic cloud. The crosstalk between the two photodetectors is found to be lower than 0.02%. The variation in the light flux is smaller than 0.5% (resp. 2.7%) over 5 mm (resp. 10 mm), which agrees perfectly with the results of simulations realized for a Lambertian source using Zemax software⁵, displayed as a thin line in the figure. We find identical behavior for the two systems. Figure 7 (right) represents with black and white squares the signal measured by the lower photodetectors when displacing

⁵ ZEMAX Development Corporation, Bellevue, WA, USA, www.zemax.com

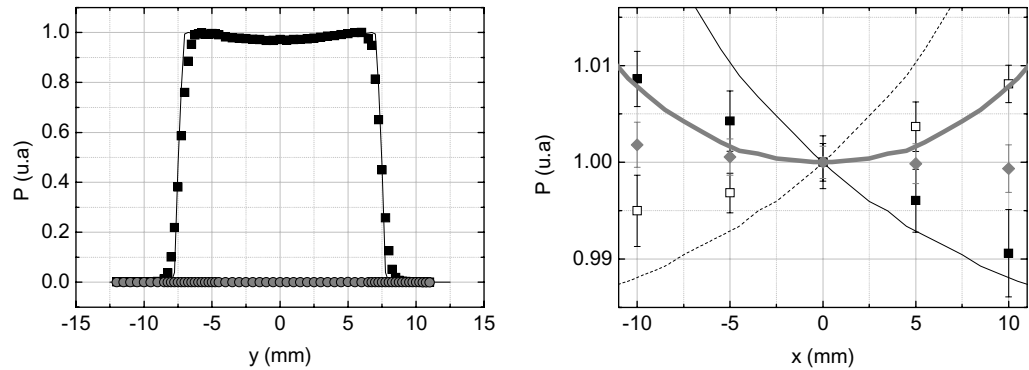


Figure 7. Study of the symmetry of the detection system. Normalized optical power measured on the photodiodes in the horizontal characterization. Left: the source is moved along the horizontal axis y , whereas z and x are constants such that the source is at the level of the center of a photodetector. Black squares and gray dots represent the experimental results for the two photodiodes of a single setup. Lines show the calculations with Zemax. Right: for both setups at the same z level as on the left for $y = 0$. Black squares for the North setup and open squares for the South setup. Thin line: calculation with Zemax. Gray diamonds: half-sum of the measurements. Gray thick line: half-sum of the calculations.

the light source along the other horizontal axis (x). We find two opposite trends, which are due to the variations in the solid angles. Summing the two signals results in a homogeneity of $\sim 0.2\%$ over 20 mm, which is significantly better than expected. The result of the simulation displayed as a thick dotted line corresponds to a 1% homogeneity over 20 mm. We attribute this discrepancy to the emission profile of the light source, which is Lorentzian rather than Lambertian.

The very good homogeneity of the fluorescence detection ensures a uniform averaging of the different transverse atomic trajectories. To give an order of magnitude, a point-like atomic cloud with a temperature of $T_{\text{at}} = 2 \mu\text{K}$ reaches a $1/e^2$ diameter of 4 mm in the detection zone. This should ensure proper averaging of the Coriolis acceleration bias to less than $1 \mu\text{Gal}$.

4.2. Coriolis shift evaluation

In [1], the Coriolis shift was determined by studying the phase of the interferometer for different rotation rates of the experimental setup as a function of the position of a detection slit that selects efficiently the atoms in velocity after a long enough time of flight. This rotation was generated by actuators and controlled by tilt-meters. In our experiment, we control the optical power in the East–West molasses beams and we rotate the device by 180° , which does not modify the systematic effects except the sign of the Coriolis bias.

The optical molasses is realized with four optical beams located in the North–South plane and two beams along the East–West direction (figure 1). Two polarizers placed on the East–West beams suppress their polarization fluctuations. The optical powers in the six beams are monitored thanks to calibrated photodiodes placed inside the molasses beam collimators, which measure a small fraction of the beams transmitted through a 45° mirror. This allows us to change the Coriolis shift by modifying the ratio of intensities of the molasses beam in the

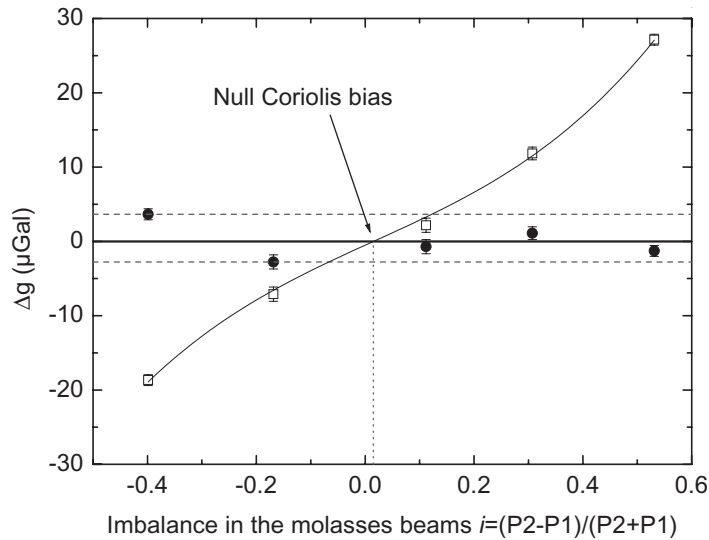


Figure 8. Combinations of the gravity values measured as a function of the imbalance in the molasses beams along the East–West direction and for two opposite orientations of the experiment. The white squares display half the difference in the signals, which corresponds to the Coriolis shift. The black circles display the half-sum and corresponds to the change in the other systematics that are all independent of the orientation of the experiment. They are dominated by the change in the wave-front aberration phase shift.

East–West direction, which changes the mean transverse velocity along this direction. Doing so, we also modify the size of the cloud and its temperature, which can change the bias due to wave-front aberrations. In order to separate the effect of the Coriolis acceleration from aberrations, we carry out the measurement of the phase of the interferometer as a function of the intensity imbalance between the molasses beam for two orientations of the experiment, which differ by 180° . We can rotate the whole experiment in less than 2 h. Since the stability of the experiment at this time scale is better than $1 \mu\text{Gal}$, we guarantee that all systematic effects remain unchanged to within $1 \mu\text{Gal}$, except for the Coriolis acceleration that changed sign. Thus, by combining the results obtained for two opposite orientations, the Coriolis acceleration shift is given by half the difference of the signals, whereas changes in the aberrations shift are given by half their sum. Figure 8 displays these linear combinations as a function of the normalized intensity difference between the molasses beams $i = (P2 - P1)/(P1 + P2)$, where $P1$ and $P2$ are the intensities of the two molasses beams in the East–West direction. We observe for half the difference an odd function, linear for a small intensity imbalance, which deviates significantly from linearity for large imbalances. This curve can be fairly well adjusted by the sum of a linear and a cubic term. The fit allows us to determine the value i_c at which the Coriolis shift vanishes. We find $i_c = 0.02(1)$, close to zero, which would correspond to equal intensities in the beams, according to the calibration of the photodiodes. We estimate an uncertainty associated with the zeroing of the Coriolis shift better than $0.4 \mu\text{Gal}$.

From the slope close to i_c , we determine a sensitivity to power imbalance of $0.2 \mu\text{Gal}$ per % of variation of the intensity ratio $r = P2/P1$. Attributing this change only to the mean velocity, this would correspond to a drift velocity of $20 \mu\text{m s}^{-1}$ per % of r , whose order of magnitude

is in reasonable agreement with previous measurements realized in [26]. But surprisingly, the sign of the effect is opposite to the expected one. In our case however, it is expected that changing r has other side effects such as shifting the cloud position and deteriorating the symmetry of the velocity distribution. Indeed, we measure relatively large position shifts when changing the intensity imbalance of the East–West beams, of about $25 \mu\text{m}$ per % of r . These displacements impact the measurement due to the residual inhomogeneity of the detection setup, whose influence is evaluated below.

For an atomic cloud perfectly centered (at $x = 0$ and $y = 0$), with a symmetric velocity distribution centered around zero, homogeneity of the detection system is not required: the symmetry of its response guarantees the cancellation. If the atomic cloud is off-centered, and/or if its mean velocity is not zero, the cancellation will no longer hold due to the inhomogeneity. In particular, the clipping of the detection zone due to the finite size of the photodiodes induces a linear dependence of $-3 \mu\text{Gal mm}^{-1}$ at $2 \mu\text{K}$ in the y -direction as it is oriented East–West for the measurement presented above. In addition, for a cloud centered in position but with a nonzero transverse velocity, this clipping leads to a reduction in the Coriolis acceleration shift by about 6% at $2 \mu\text{K}$. These effects are too small to explain the inverted behavior that we observe. We believe that this inversion, which we cannot explain, could be due to asymmetries in the velocity distribution that depend on the intensity ratio r . In general, effects due to the detection inhomogeneity will be more pronounced for higher temperatures but can be reduced by rotating the experiment by 90° in order to take advantage of the better homogeneity along the x -axis.

Anyway we believe that whatever the source of the Coriolis shift (mean velocity, detection homogeneity and asymmetry of the velocity distribution), rotating the experiment by 180° allows us to determine the correction to be applied to eliminate the Coriolis shift even for a nonoptimal imbalance $i \neq i_c$. For that we provide that all other parameters remain unchanged (such as for instance tilt, height and position), which we control to better than the μGal level.

Note that for the other linear combination of the data (the half-sum), we see resolved changes, which can be as large as $6 \mu\text{Gal}$ (black dots in figure 8). We attribute them to the changes in aberration phase shift induced by position and velocity modifications.

4.3. Stability of the cloud position, and the effect on g

In the previous section, we have shown that the measured g value was affected by the East–West MOT beams' intensity ratio r , not only because of the Coriolis effect, but also because of the change in atomic position and velocity distributions induced by imbalanced intensities. Correcting the g measurements from the influence of changes in the intensity ratio r allows us to improve the long-term stability. We applied such a correction in the case of the measurement shown in figure 2, using the measurement of r at each cycle, and taking into account the measured sensitivity of $24(2) \mu\text{Gal}$ per unit of r in this particular orientation of the experimental setup. We expect the latter effect to be also present for intensity imbalances in the other two pairs of trapping beams lying in the North–South plane.

We measure the sensitivity of g to the power imbalance in the North–South MOT beams, and found variations significantly different for the two pairs: $36(7) \mu\text{Gal}$ per unit of r_{NS1} for one pair of the North–South beams and $-5(2) \mu\text{Gal}$ per unit of r_{NS2} for the other pair. To understand how the cloud is modified for different power intensity ratios, we perform a fluorescence detection of the atoms using the CCD camera from the North–West direction (figure 1). We point out that the position measurements are only sensitive to displacements in

the North–East/South–West plane, orthogonal to the camera axis. We assume that a change in the intensity ratio of two counter-propagating beams induces a displacement mainly in the light propagation direction. For the MOT beams oriented in the East–West direction, we measure a position sensitivity of $25 \mu\text{m}$ per % of the intensity ratio r . For the North–South MOT beams, where the laser intensity is larger, we find sensitivities of $160 \mu\text{m}$ in the North–South direction per % of r_{NS1} , and $-27 \mu\text{m}$ per % of r_{NS2} . Although the effect of each pair of beams in the North–South direction is quite different when expressed as a function of intensity ratios, we find comparable sensitivities when expressed as a function of the position of about $2 \mu\text{Gal mm}^{-1}$.

The power ratios of all three pairs of MOT beams slowly fluctuate with time. A monitoring over 50 h of the NS1 beams showed a drift as large as 3% in r_{NS1} . This amounts to a g variation of $1 \mu\text{Gal}$ over the same time interval, if we assume that only this pair of beams exhibits intensity ratio fluctuations. Given that the other pairs of beams also fluctuate in intensity and that there are also polarization fluctuations that we have not considered, this could explain the slow fluctuations in the g residuals with an amplitude of a few μGal shown in figure 2.

Over the 10 month period corresponding to the data displayed in figure 4, the intensities in the molasses beams have been frequently measured (only r is recorded continuously throughout the measurements). We found fluctuations in the North–South ratios of up to 10% peak to peak, which correspond to g fluctuations of up to $4 \mu\text{Gal}$. However, we found fluctuations in r_{NS1} significantly lower (3% peak to peak) over the last four months, which correspond to g fluctuations of up to $1 \mu\text{Gal}$ only. Repeated measurements of the cloud initial position were also carried out with the CCD camera during the same four month period. We found position variations of about $300 \mu\text{m}$, similar along the two axes of the camera, in agreement with expected fluctuations. From those observations we draw two conclusions. Firstly, effects due to polarization fluctuations in the North–South beams, which we are not able to measure, are at most of the same order of magnitude as intensity fluctuations. Secondly, during the last four month period, position fluctuations represent a significant contribution to the g fluctuations in figure 4.

4.4. Estimation of the optical aberrations bias

The measured value of g is affected by a bias due to the nonplanarity of the Raman optical wave-front, originating from the imperfections of the retro-reflecting mirror and of the quarter-wave plate placed at the bottom of the vacuum chamber. The central parts ($11 \times 11 \text{ cm}^2$) of these two optical elements have been characterized with a Shack Hartmann wave-front analyzer before being inserted into the vacuum chamber. A planarity of $\lambda/15$ peak to valley and $\lambda/100$ rms was measured for the central part of the mirror, from which we could predict a bias on g of $-2 \mu\text{Gal}$ at $T_{\text{at}} = 2 \mu\text{K}$. A similar characterization of the quarter-wave plate gave a bias of $2.5 \mu\text{Gal}$, leading to a global effect of $0.5 \mu\text{Gal}$. However, the mirror and plate have probably undergone mechanical strains when clamped inside the UHV chamber, invalidating these preliminary planarity measurements. Moreover, the quality of these optics cannot be measured *in situ*. Instead, in order to gain insights into the amplitude of this effect, we measure the dependence of g on the atomic temperature T_{at} . Indeed, the higher the temperature, the larger the area of the optical wave-front being probed. The unbiased g value corresponds to the case of a nonexpanding atomic cloud and can be obtained by extrapolating the measurements to zero temperature.

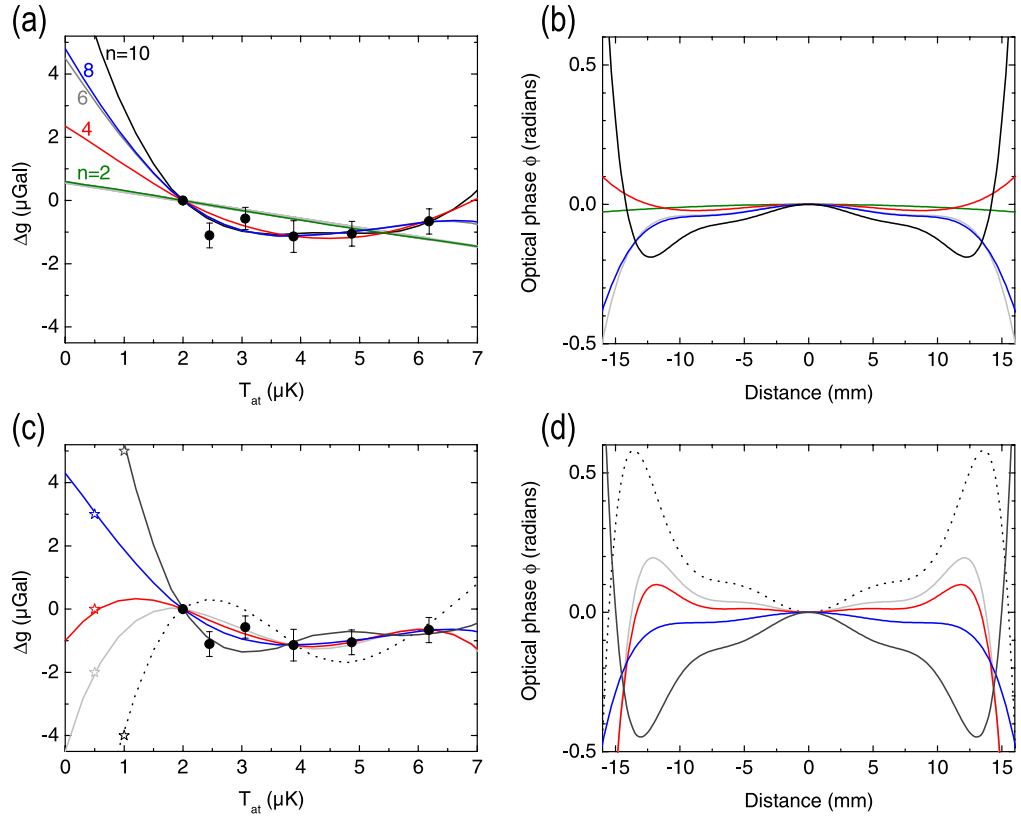


Figure 9. Black circles on (a) and (c): experimental values of $g(T_{\text{at}}) - g(2\mu\text{K})$. (a) Fit to the data with subsets of Zernike polynomials ($Z_{n \leq n_{\text{max}}}^0$) for increasing n_{max} . The linear fit, represented as a gray line, coincides with the fit corresponding to $n_{\text{max}} = 2$. (b) Reconstructed wave-fronts. (c) Fits with the subset corresponding to $n_{\text{max}} = 10$ for different added fake points (stars) below $2\mu\text{K}$. (d) Reconstructed wave-fronts.

In figure 9, we display as black circles the experimental measurements of g for different atomic temperatures between 2 and $6\mu\text{K}$. Each data point is obtained by carrying out at least 3000 measurements of g in four different configurations. In configurations 1 and 2, the atomic temperature is kept at $T_{\text{at}} = 2\mu\text{K}$. In configurations 3 and 4, the atomic temperature is set to another value by adjusting the detuning of the molasses beams during the sub-Doppler cooling phase. Configurations 1 and 3 are performed with k_{\uparrow} pointing upwards, and configurations 2 and 4 with k_{\downarrow} pointing downwards. In all four configurations, the Rabi frequency of the Raman pulses is kept at its nominal value Ω_{eff} . This way, according to the algorithm described in section 3.2, we measure $(\Delta\Phi_{\uparrow} - \Delta\Phi_{\downarrow})/2$ for two temperatures, while rejecting the effects that are independent of the direction of k_{eff} . Changes in the two-photon light shift with atomic temperature are negligible. In this measurement, which is realized in a given orientation, we cannot exclude a contribution of the Coriolis shift, which can depend on the atomic temperature. All other systematic effects (such as tidal variations and polar motion) are canceled, since they exhibit slow variations compared to the alternation between the four configurations.

We find small changes, $1\mu\text{Gal}$ at most, in the explored temperature range. Considering the statistical uncertainties of the order of $0.5\mu\text{Gal}$, differences between the measurements are

hardly resolved. Additionally, as those measurements were carried out over a few days, they could be affected by differences due to changes in cloud position. First, let us consider the simple case where the wave-front is a pure curvature that leads to a linear dependence (equation (6)). The extrapolation of the linear fit, displayed as a gray line in figure 9(a), leads to a bias in g equal to $0.6(5) \mu\text{Gal}$. Although compatible with the data considering their uncertainties, this linear fit is not relevant since the wave-front could be more complex than a curvature.

Figure 9(a) displays as lines the fit obtained when expressing the wave-front as a linear combination of increasing subsets of cylindrically invariant Zernike polynomials Z_n^0 (with $n \leq n_{\text{max}}$) defined on a 30 mm radius disc. The lines correspond to $n_{\text{max}} = 2, 4, 6, 8$ and 10. The contribution of each polynomial results from a convolution over the spatial and velocity distributions as well as with the detection efficiency (figure 7). For this calculation, we assumed that the initial cloud position coincides with the Zernike disc center and that the cloud expands symmetrically around its initial position, which is why only cylindrically invariant polynomials contribute. Increasing n_{max} leads to larger extrapolated values up to $9 \mu\text{Gal}$ without a very significant reduction in the residuals as soon as $n_{\text{max}} \geq 4$. Figure 9(b) presents the associated reconstructed wave-fronts that exhibit larger phase variations across the radius with increasing n .

In order to further illustrate the difficulty of extrapolating the measurements to zero temperature, we made similar fits with $n_{\text{max}} = 10$ after adding to the data supplementary fake points below $2 \mu\text{K}$, which are displayed in figure 9(c) as stars. Remarkably, most of the corresponding fits (displayed as lines in figure 9(c)) agree reasonably well with the experimental data, even though they correspond to very different biases on g , ranging from -4 to $15 \mu\text{Gal}$. Even larger biases are compatible with the data if we include Zernike polynomials with orders larger than $n = 10$ in the wave-front model but this leads to larger phase deviations from the nominal quality of the optics.

Although the spatial atomic distribution averages the fast wave-front structures (see figure 10), for a cloud with a size $\sigma = 600 \mu\text{m}$ and a temperature $T_{\text{at}} = 2 \mu\text{K}$, polynomials with large $n \leq 50$ are still not completely averaged out by the atomic spatial distribution. In our case, measurements with twice larger clouds show no significant difference which is expected if the wave-front is dominated by relatively low-order polynomials ($n \lesssim 20$). Measurements with even larger sizes would provide a quantitative criterion for truncating the basis for Zernike polynomials in our analysis.

As a conclusion, this study indicates that a simple linear extrapolation of $g(T_{\text{at}})$ at zero temperature does not give a reliable aberrations bias estimation. In fact, deriving the exact wave-front shape via measurements of g is a difficult mathematical task, equivalent to an interpolation problem, where additional degrees of freedom will always give a better fit. Although the hypotheses formulated for the calculation are unrealistic (no change in the initial position distribution and symmetric expansion), this does not invalidate the conclusion we draw here. In particular, the study shows that given the uncertainties in our measurements, even relatively small (less than $1 \mu\text{Gal}$), reaching a comparable uncertainty in the extrapolation is difficult. Measurements with a better resolution over a larger temperature range would give better constraints. In that case however, the question remains whether the long-term stability on these differential measurements allows for it and/or if we are able to account for the influence of the Coriolis acceleration shift and detection clipping over the whole temperature range.

A complementary way to overcome this issue is to get more information concerning the Raman optical wave-front, for example by sampling the wave-front differently by changing

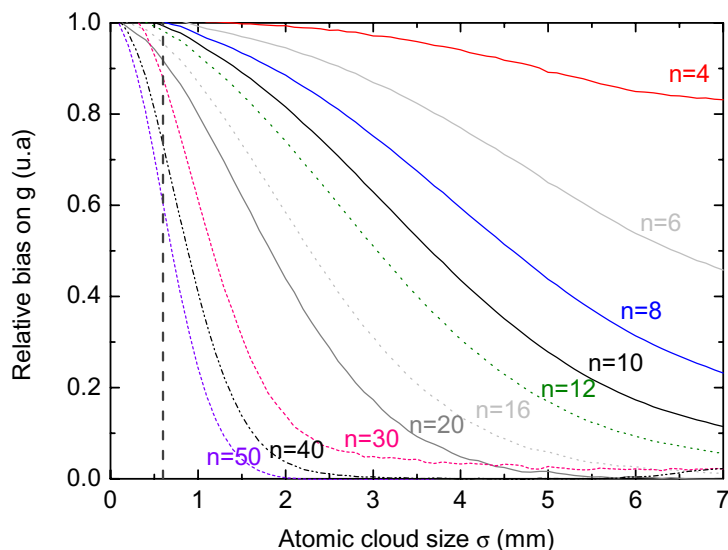


Figure 10. Relative bias on gravity measurements for an optical wave-front given by the Zernike polynomial Z_n^0 defined on a 30 mm radius disc, for different values of n . As n increases, the wave-front exhibits faster spatial variations, which are better averaged for large cloud sizes. All lines are normalized to the g bias calculated for an atomic cloud with $\sigma = 0$. Vertical dashed line: measured initial atomic cloud size $\sigma = 600 \mu\text{m}$.

the interferometer time T , or by modifying the initial cloud position, velocity and size. In any case, the faithful reconstruction of the wave-front will require us to truncate the Zernike polynomial basis, based on physical arguments: for instance, the wave-front shape obtained with the unmounted optics was found to be dominated by low-order contributions, and mechanical constraints when mounted are not expected to lead to large modifications of the high-order contributions.

Finally, even if the data suggest that the effect does not depend much on temperature as expected for small wave-front distortions, a faithful extrapolation is not possible. We thus apply a null correction for the effect of the wave-front distortions, with an uncertainty expanded to $4 \mu\text{Gal}$, which is much larger than the expected value extracted from the characterization of the optics.

5. Conclusion

We have described the main features of our new-generation cold atom gravimeter. In particular, we have presented our measurement protocol, which allows us to reject a large fraction of the systematic effects at the price of a reduction in sensitivity. A continuous measurement over 12 days has been presented, which shows excellent agreement with a model for tidal gravity changes. The long-term stability of the tide-corrected gravity signal reaches $1 \mu\text{Gal}$ after 5000 s, and remains below that level for longer times. Measurements over a 10 month period show g fluctuations of $3 \mu\text{Gal}$ standard deviation.

We have studied the effect of Coriolis acceleration and wave-front distortions, which arise from the transverse motion of the atoms. A dedicated optical system for the fluorescence

Table 1. Corrections and uncertainties affecting the 12-day CAG g measurement presented in this paper. ‘Other effects’ corresponds to systematic shifts, which are not detailed in this paper such as due to the vertical gravity gradient [1], self-gravity effect [27], frequency reference offsets, etc. Environmental biases being time dependent (td), we display the mean value of these effects over the total duration of the measurement.

	Effect	Bias (μGal)	U (μGal)
Environmental	Tidal model (td)	−18.8	0.5
	Atmospheric pressure (td)	−1.7	0.5
	Polar motion (td)	−3.8	0.1
	<i>Total</i>	−24.3	0.7
Device	Other effects	−12.1	0.8
	\vec{k}_{indep}	0.0	0.1
	Tilt	4.2	0.5
	LS2	−12.3	0.5
	Coriolis	0.5	0.4
	WF aberrations	0.0	4.0
	<i>Total</i>	−19.7	5.1
	<i>Total</i>	−44.0	5.2

detection of the interferometer output ports has been described, which guarantees the homogeneity in the collection efficiency at the % level across the atomic cloud. This allows for uniform weighting over the different transverse trajectories. Thanks to the mobility of the experimental setup, the Coriolis shift has been evaluated as a function of the molasses beam imbalance, from the combination of measurements realized with two opposite orientations with respect to the Earth’s rotation orientation. The associated uncertainty has been evaluated to $0.4 \mu\text{Gal}$. Moreover, we have realized g measurements for increasing temperatures, in order to probe the wave-front of the Raman lasers. We have shown the difficulty of extrapolating such measurements to zero temperature, and correcting for the bias due to wave-front distortions even though our results show small sensitivity to changes in the temperature and size of the atomic cloud. This last effect leads to an uncertainty of $4.0 \mu\text{Gal}$, which dominates the complete accuracy budget of the device ($5.2 \mu\text{Gal}$) as presented in table 1.

In order to improve the long-term stability, better control of the MOT laser intensities and polarizations will be necessary in order to improve the stability of the initial position and velocity of the atomic source. In addition, careful continuous monitoring of environmental perturbations should be done such as water table level and soil moisture, which can generate variations up to $15 \mu\text{Gal}$ [28–30]. In order to perfect the accuracy budget of the device, an accurate determination of the wave-front distortion effect is to be performed. Additional measurements with a better resolution and for different positions, sizes and velocities of the atomic cloud would allow us to draw a complete map of the effects in the parameter space from which a faithful reconstruction of the wave-front is in principle possible. This appears to be a very tedious task that requires perfect control of those parameters. We believe a more attractive method consists in using colder samples for better extrapolation to zero temperature,

obtained with either horizontal velocity selection or evaporative cooling in a dipole trap [31]. Both approaches will be implemented on our gravimeter in the near future.

Acknowledgments

The authors are grateful to David Horville from GEPI at Observatoire de Paris for the realization of the optical detection setups and to the entire ‘Mechanics’ team for support in the design and construction of the experimental chamber. The research within this EURAMET joint research project leading to these results has received funding from the European Community’s Seventh Framework Program, ERA-NET Plus, under grant agreement no. 217257, and from IFRAF (Institut Francilien de Recherche sur les Atomes Froids). QB thanks CNES for support.

References

- [1] Peters A, Chung K Y and Chu S 2001 High-precision gravity measurement using atom interferometry *Metrologia* **38** 25–61
- [2] Marson I and Faller J E 1986 g —the acceleration of gravity: its measurement and its importance *J. Phys. E: Sci. Instrum.* **19** 22–32
- [3] Genevès G *et al* 2005 The BNM watt balance project *IEEE Trans. Instrum. Meas.* **54** 850–3
- [4] Varoquaux G, Nyman R A, Geiger R, Cheinet P, Landragin A and Bouyer P 2009 How to estimate the differential acceleration in a two-species atom interferometer to test the equivalence principle *New J. Phys.* **11** 113010
- [5] Bouyer P and Landragin A 2009 *Patent No.* WO/2009/118488 A2 (published on 1 October 2009)
- [6] Bodart Q, Merlet S, Malossi N, Pereira Dos Santos F, Bouyer P and Landragin A 2010 A cold atom pyramidal gravimeter with a single laser beam *Appl. Phys. Lett.* **96** 134101
- [7] Le Gouët J, Mehlstäubler T E, Kim J, Merlet S, Clairon A, Landragin A and Pereira Dos Santos F 2008 Limits to the sensitivity of a low noise compact atomic gravimeter *Appl. Phys. B* **92** 133–44
- [8] 2009 *ICAG’09 (International Comparison of Absolute Gravimeters) at BIPM in 2009* unpublished
- [9] Merlet S, Bodart Q, Malossi N, Landragin A, Pereira Dos Santos F, Gitlein O and Timmen L 2010 Comparison between two mobile absolute gravimeters: optical versus atomic interferometers *Metrologia* **47** L9–11
- [10] Louchet-Chauvet A, Merlet S, Bodart Q, Landragin A, Pereira Dos Santos F, Baumann H, D’Agostino G and Origlia C 2011 Comparison of 3 absolute gravimeters based on different methods for the e-MASS project *IEEE Trans. Instrum. Meas.* at press (arXiv:1008.2884)
- [11] Kasevich M and Chu S 1991 Atomic interferometry using stimulated Raman transitions *Phys. Rev. Lett.* **67** 181–4
- [12] Bordé Ch J 1989 Atomic interferometry with internal state labelling *Phys. Lett. A* **140** 10–2
- [13] Bordé Ch J 2001 Theoretical tools for atom optics and interferometry *C. R. Acad. Sci. Paris, t.2, Série IV* 509–30
- [14] Guirk J M, Foster G T, Fixler J B and Kasevich M A 2001 Low-noise detection of ultracold atoms *Opt. Lett.* **26** 364–66
- [15] Guirk J M, Foster G T, Fixler J B, Snadden M J and Kasevich M A 2002 Sensitive absolute-gravity gradiometry using atom interferometry *Phys. Rev. A* **65** 033608
- [16] Moler K, Weiss D S, Kasevich M A and Chu S 1992 Theoretical analysis of velocity-selective Raman transition *Phys. Rev. A* **45** 342–8
- [17] Baillard X, Gauguet A, Bize S, Lemonde P, Laurent Ph, Clairon A and Rosenbusch P 2006 Interference-filter-stabilized external-cavity diode lasers *Opt. Commun.* **266** 609–13

- [18] Gauguet A, Mehlstäubler T E, Lévêque T, Le Gouët J, Chaibi W, Canuel B, Clairon A, Pereira Dos Santos F and Landragin A 2008 Off-resonant Raman transition impact in an atom interferometer *Phys. Rev. A* **78** 043615
- [19] Merlet S, Kopaev A, Diament M, Genevès G, Landragin A and Pereira Dos Santos F 2008 Micro-gravity investigations for the LNE watt balance project *Metrologia* **45** 265–74
- [20] Xu G (ed) 2010 *Science of Geodesy, Advances and Future Directions* 1st edn (Berlin: Springer) ISBN: 978-3-642-11740-4
- [21] Merlet S, Francis O, Palinkas V, Kostelecky J, Le Moigne N, Jacobs T and Genevès G 2007 Absolute gravity measurement at LNE (TG-SMM 2007) *Symp. Proc. (St Petersburg, Russia)* p 173–4
- [22] Sagnac G 1913 L'éther lumineux démontré par l'effet vent relatif d'éther dans un interféromètre en rotation uniforme *C. R. Acad. Sci. Paris* **157** 708
- [23] Riehle F, Kisters Th, Witte A, Helmcke J and Bordé Ch. J 1991 Optical Ramsey spectroscopy in a rotating frame: Sagnac effect in a matter-wave interferometer *Phys. Rev. Lett.* **67** 177–80
- [24] Weiss D S, Young B C and Chu S 1994 Precision measurement of \hbar/mCs based on photon recoil using laser-cooled atoms and atomic interferometry *Appl. Phys. B* **59** 217–56
- [25] Laikin M 2007 *Lens Design* 4th edn (Boca Raton, FL: CRC Press) ISBN 978-0-8493-8278-9 pp 79–86
- [26] Gauguet A, Canuel B, Lévêque T, Chaibi W and Landragin A 2009 Characterization and limits of a cold-atom Sagnac interferometer *Phys. Rev. A* **80** 063604
- [27] D'Agostino G, Merlet S, Landragin A and Pereira Dos Santos F 2011 Perturbations of the local gravity field due to mass distribution on precise measuring instruments: a numerical method applied to a cold atom gravimeter *Metrologia* at press (arXiv:1105.2173)
- [28] Jacob T, Chery J, Bayer R, Le Moigne N, Boy J-P, Vernant P and Boudin F 2009 Time-lapse surface to depth gravity measurements on a karst system reveal the dominant role of the epikarst as a water storage entity *Geophys. J. Int.* **178** 347–60
- [29] Naujoks M, Weise A A, Kroner C C and Jahr T 2007 Detection of small hydrological variations in gravity by repeated observations with relative gravimeters *J. Geod.* **82** 543–53
- [30] Van Camp M, Williams S D P and Francis O 2005 Uncertainty of absolute gravity measurements *J. Geophys. Res.* **110** B05406
- [31] Clément J F, Brantut J P, Robert-de-Saint-Vincent M, Nyman R A, Aspect A, Bourdel T and Bouyer P 2009 All-optical runaway evaporation to Bose–Einstein condensation *Phys. Rev. A* **79** 061406